C≡N vacancy engineering of Prussian blue analogs for the advanced oxygen evolution reaction

Wenhao Deng[a], *Qiangqiang Zhao*[a], *Baochai Xu*[a], *Song Xie*[a], *Weihong Jin*[b], *Xuming Zhang*[c], *Biao Gao*[c], *Zhitian Liu*[a], *Zaenab Abd-Allah*[d], *Paul K Chu*[e], *Xiang Peng*[a]*

[a] Hubei Key Laboratory of Plasma Chemistry and Advanced Materials, Hubei Engineering Technology Research Center of Optoelectronic and New Energy Materials, School of Materials Science and Engineering, Wuhan Institute of Technology, Wuhan, 430205, China

[b] Institute of Advanced Wear & Corrosion Resistant and Functional Materials, Jinan University, Guangzhou, 510632, China

[c] State Key Laboratory of Refractories and Metallurgy and Institute of Advanced Materials and Nanotechnology, Wuhan University of Science and Technology, Wuhan, 430081, China

[d] Department of Engineering, Manchester Metropolitan University, John Dalton Building, Manchester M15 6BH, United Kingdom

[e] Department of Physics, Department of Materials Science and Engineering, and Department of Biomedical Engineering, City University of Hong Kong, Tat Chee Avenue, Kowloon, Hong Kong, China

* Correspondence: xpeng@wit.edu.cn

Abstract: Hydrogen production by electrocatalytic water splitting suffers from the sluggish kinetics of the oxygen evolution reaction (OER) and large power consumption and hence, efficient OER electrocatalysts are required to enhance the energy conversion efficiency. Vacancies can be used to create active unsaturated coordination, regulate the electronic structure, and enhance the charge transfer efficiency to improve both the intrinsic and extrinsic catalytic activities. This work aims to construct an efficient OER electrocatalyst through a precise control of the C≡N vacancies ($V_{C\equiv N}$) in NiFe- and NiCo-PBAs leading to outstanding OER characteristics and improved energy conversion efficiency. The amount of $V_{C\equiv N}$ can be regulated precisely *via* thermal treatment. The electronic interactions occur between Ni and Fe sites during introduction of $V_{C\equiv N}$. As a result, the synergistic effects of Ni-Fe electronic interactions and $V_{C\equiv N}$ lead to outstanding OER characteristics such as a small overpotential of 270 mV to achieve a high current density of 50 mA cm^{-2} as well as excellent stability for 80 h at a high current density of 100 mA cm^{-2}, which are better than those of the pristine PBAs electrocatalyst. The results demonstrate a precise strategy to produce $V_{C\equiv N}$ in PBAs-based electrocatalysts for advanced OER and efficient hydrogen production.

Keywords: C≡N vacancy; Prussian blue analogs (PBAs); oxygen evolution reaction; water spitting; hydrogen production

1. Introduction

Clean and sustainable energy is essential to combating climate change. Electrochemical water splitting is a promising mean to produce pure hydrogen for clean energy generation [1-3]. Water electrolysis consists of the hydrogen evolution reaction (HER) on the cathode and oxygen evolution reaction (OER) on the anode and the slow kinetics of OER is usually the bottleneck limiting the efficiency [4, 5]. Noble metal-based catalysts such as IrO_2 and RuO_2 have been applied to facilitate OER but the high cost and low reserve are huge barriers against commercial adoption [6, 7]. Therefore, economical and high-activity non-noble metal-based electrocatalysts are imperative to advanced OER.

Abundant metals such as Ni, Co, and Fe and their compounds have been proposed to enhance OER. For example, Ni and its compounds such as Ni metals [8, 9], $NiSe_2$ [10, 11], NiO [12, 13], and NiFeO [14] can drive OER at low overpotentials. An electrocatalyst consisting of Ni-FeO_x and $FeNi_3$ prepared on nickel foam (Ni-FeO_x/$FeNi_3$/NF) requires 269 mV to yield a current density of 50 mA cm^{-2} in OER and shows good stability for more than 200 h [14]. The crystal structure of the electrocatalysts is also crucial to the performance. The Prussian blue analogs (PBAs) are considered promising electrocatalysts for OER due to the tunable structure and composition [15]. PBAs are perovskite-type materials with the general formula of $A_xM_1[M_2(CN)_6]_y \cdot mH_2O$, where A stands for an alkali metal such as Na and K and M_1 and M_2 are transition metals such as Ni, Co, Fe, etc. [16, 17]. Bimetallic electrocatalysts composed of nickel and iron have been reported to have good OER

activity [18, 19]. For example, Wu *et al* have prepared bimetallic Ni-Fe selenide from NiFe-PBAs with an optimized electronic structure that exhibits synergistic effects between Ni and Fe and has good OER characteristics [19]. However, the CN species which account for a larger proportion of PBAs do not play a significant role in OER.

Generally, PBAs are composed of M_2–C≡N–M_1 units with strong C≡N bonds and relatively weak M_2–C and M_1–N bonds [20]. Hence, it is possible to break the M_2–C and M_1–N bonds directionally with a moderate energy to produce C≡N vacancies ($V_{C≡N}$) in PBAs. Vacancy engineering is in fact an effective strategy to generate active unsaturated coordination [21], regulate the electronic structure [22, 23], and enhance the charge transfer efficiency [24] to improve both the intrinsic and extrinsic catalytic activities. $V_{C≡N}$ could be created in PBAs by a plasma treatment [20, 25]. Yu et al. have studied the OER characteristics of $V_{C≡N}$-mediated PBAs, which exhibit a low overpotential of 283 mV at 10 mA cm^{-2} that is better than those of the original PBAs and previously reported OER electrocatalysts with vacancies [20]. However, plasma processing typically requires a complex apparatus and bond breaking tends to be random. Therefore, a more precise and easier technique to produce $V_{C≡N}$ in PBAs is important albeit challenging.

Herein, a strategy of precisely regulating the $V_{C≡N}$ in NiFe-PBAs *via* a mild thermal treatment is described, as illustrated in **Scheme 1**. The amount of $V_{C≡N}$ in NiFe-PBAs can be adjusted precisely by controlling the treatment temperature. NiFe-PBAs with different $V_{C≡N}$ concentrations can be prepared and electronic interactions between Ni and Fe sites are introduced. The synergistic effects rendered by the Ni-Fe

electronic interactions and $V_{C\equiv N}$ give rise to outstanding OER characteristics such as a small overpotential of 270 mV to reach a current density of 50 mA cm^{-2} in addition to good stability of 80 h at a high current density of 100 mA cm^{-2}, which are better than those of the pristine PBAs electrocatalysts. Moreover, this mild thermal treatment can be extended to other PBAs-based electrocatalyst (NiCo-PBAs).

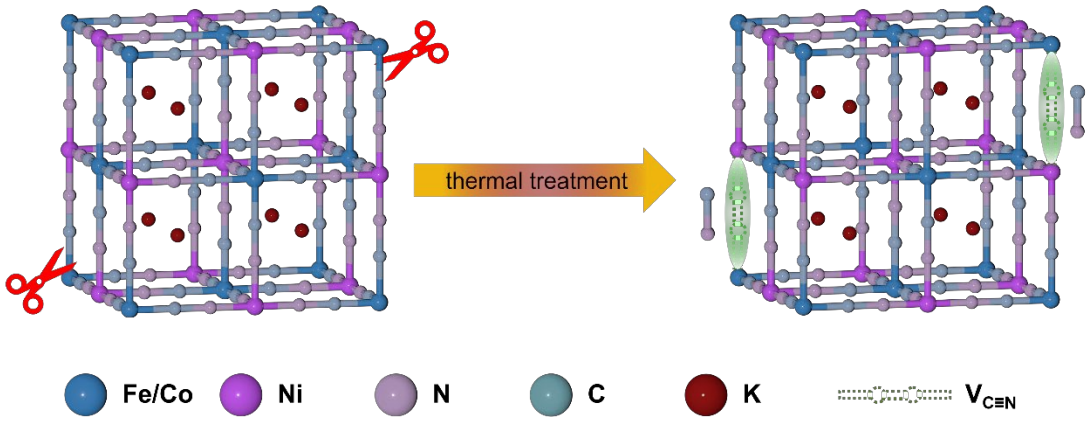

Scheme 1. C≡N vacancy engineering of PBAs.

2. Experimental Details

2.1 Materials Preparation

2.4 mmol $NiCl_2$ and 3.6 mmol $Na_3C_6H_5O_7 \cdot 2H_2O$ were dissolved in 80 mL of deionized water (DW) to obtain solution A and then 1.6 mmol $K_3Fe(CN)_6$ was dissolved in 80 mL of DW water to produce solution B. Solution A was added to solution B dropwise under stirring. A piece of clean carbon cloth (CC, 5×6 cm^{-2}) was immersed in the mixture for 24 h and then rinsed with distilled water and ethanol several times before vacuum drying. The product was designated as NiFe-PBAs.

To regulate the C≡N ligands, NiFe-PBAs was thermally treated at 200, 250, and

300 ºC in a tube furnace under N_2 at a rate of 5 ºC min^{-1} for 2 h, respectively. The products were designated as PBAs-200, PBAs-250, and PBAs-300, where the numbers indicate the treatment temperature. NiCo-PBAs was prepared by the same protocol as NiFe-PBAs except replacing $K_3Fe(CN)_6$ with $K_3Co(CN)_6$. NiCo-PBAs was thermally treated in a tube furnace under N_2 to produce NiCo-PBAs-V.

2.2 Materials Characterization

A scanning electron microscope (SEM, FEI/Philips XL30 Esem-FEG) was used to characterize the morphology of the samples. The crystal structure of the samples was determined by the X-ray diffraction (XRD, LabX-6100, Shimadzu). Raman scattering (HR RamLab) was conducted to analyze the chemical bonding and X-ray photoelectron spectroscopy (XPS, Thermo Scientific K-Alpha+, Thermo Fisher) with monochromatic Al Kα X-ray was performed to determine the chemical states referenced to the C 1*s* peak at 284.8 eV.

2.3 Electrochemical Assessment

The electrochemical measurements were carried out in 1 M KOH on the CHI 660E electrochemical workstation (Shanghai CH Instrument, China). The typical three-electrode system consisted of a graphite rod, saturated calomel electrode, and PBAs modified CC as the counter electrode, reference electrode, and working electrode, respectively. All the potentials in OER were *iR* corrected and referenced to the reversible hydrogen electrode (RHE) according to Nernst equation E(RHE) = E(SCE)

+ 0.242 + 0.059 × pH. The pH of 1 M KOH solution was measured to be 13.62 by a pH meter (FE, Mettler Toledo). Linear sweep voltammetry (LSV) was performed at a scanning rate of 5 mV s^{-1} to obtain the polarization curves. The Tafel slope was plotted as potentials (V) *vs*. log currents (log|*j*|) based on the polarization curves. The electrochemical active surface area (ECSA) was obtained by measuring the electrochemical double-layer capacitance (C_{dl}) based on the cyclic voltammetry (CV) curves measured at different scanning rates of 10~100 mV s^{-1}. Electrochemical impedance spectroscopy (EIS) was carried out at an initial potential of 0.5 V *vs*. SCE. The long-term durability was evaluated by continuous chronopotentiometry at a current density of 100 mA cm^{-2} and O_2 production was measured by the water displacement method.

3. Results and Discussion

3.1. Structure and composition study

NiFe-PBAs prepared on carbon cloth by heterogeneous nucleation with a chelating agent [26, 27] contain Fe–C≡N–Ni units with strong C≡N bonds and relatively weak Fe–C and Ni–N bonds [20]. The thermal treatment cleaves the Fe–C and Ni–N bonds in the Fe–C≡N–Ni units due to the higher activation barrier of cleaving the C≡N bonds as illustrated in **Scheme 1**. The generated C≡N then moves away from the PBA lattices to form the $V_{C\equiv N}$ [28, 29].

The morphology of the samples is examined by scanning electron microscopy (SEM), as shown in **Figure 1**. **Figure 1a** shows that the NiFe-PBAs precursor has the

morphology of nanocubes with a smooth surface and side length of ~150 nm distributed uniformly on CC. After the thermal treatment at 200-300 °C, the nanocube morphology is maintained well as revealed in **Figures 1b-d**. When the temperature is 300 °C, the surface of the nanocubes became rough and porous as shown in **Figure 1d**. The porous structure is formed by escape of C≡N species from NiFe-PBAs at the high temperature.

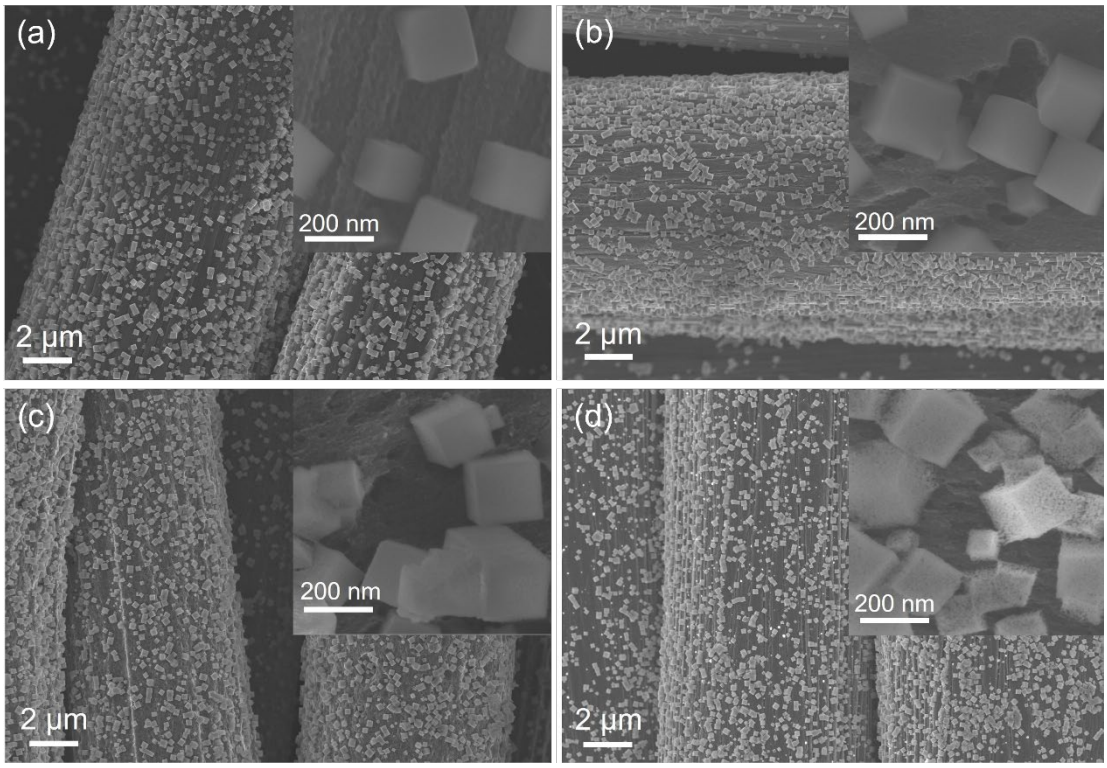

Figure 1. SEM images of (a) NiFe-PBAs, (b) PBAs-200, (c) PBAs-250, and (d) PBAs-300.

The Raman scattering spectra in **Figure 2a** disclose two main peaks at 2,160 and 2,189 cm^{-1}, corresponding to C≡N vibrations of Fe^{2+}–C≡N–Ni^{2+} and Fe^{3+}–C≡N–Ni^{2+}, respectively [30]. The peak at 2,189 cm^{-1} weakens with increasing the temperature

compared to the NiFe-PBAs precursor, indicating decrease of C≡N and generation of $V_{C\equiv N}$ in NiFe-PBAs. The peaks at 2,160 and 2,189 cm^{-1} of PBAs-300 almost disappear suggesting the $V_{C\equiv N}$ is generated in Fe^{3+}–C≡N–Ni^{2+} and Fe^{2+}–C≡N–Ni^{2+} at a higher temperature, thus confirming generation of $V_{C\equiv N}$ after the thermal treatment. **Figure 2b** shows that the diffraction peaks can be indexed to $KNiFe(CN)_6$ (JCPDS card No. 51-1897). The diffraction peaks decreases with increasing the temperature possibly because of structural distortion arising from the generation of $V_{C\equiv N}$ [31].

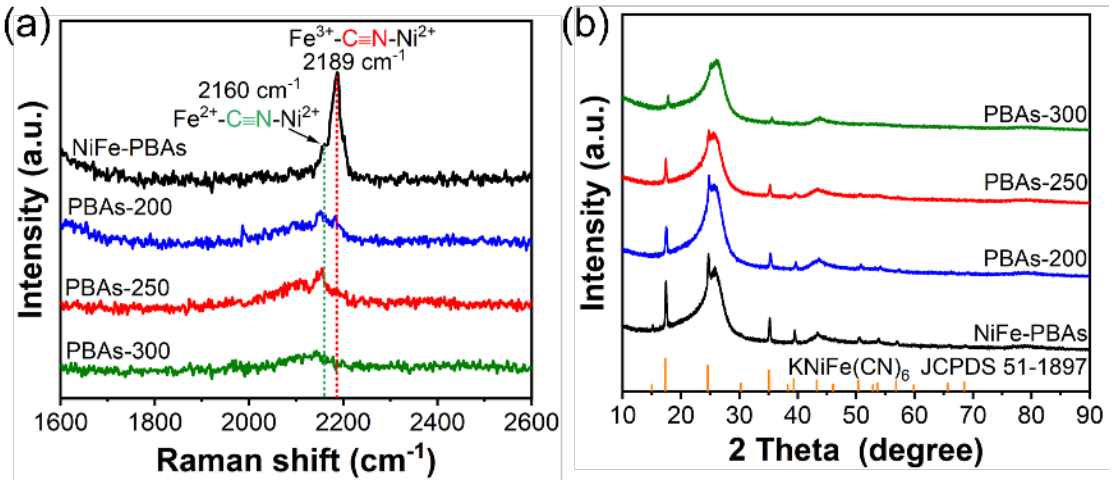

Figure 2. (a) Raman scattering spectra and (b) XRD spectra of NiFe-PBAs, PBAs-200, PBAs-250, and PBAs-300.

The chemical composition and chemical states are determined by X-ray photoelectron spectroscopy (XPS). **Figure S1** discloses the presence of C, N, Ni, and Fe. The peaks at 874.1, 876.1, and 880.7 eV in **Figure 3a** can be ascribed to Ni(II), Ni(III), and satellite peak of Ni $2p_{1/2}$, respectively. **Figure 3b** shows the peaks at 721.5, 724.0, and 725.0 eV originate from Fe-C, Fe(II), and Fe(III) of Fe $2p_{1/2}$, respectively.

As the processing temperature goes up, the surface Ni(III) concentration decreases but the Fe(III) concentration increases as shown in **Figure 3c**. The results reveal electronic interactions between the Ni and Fe atoms during the thermal treatment and electrons are transferred from Fe to Ni atoms, in agreement with findings by Yu. *et.al.* [20]. The Fe sites with higher oxidation states have a stronger ability to adsorb OH^- and consequently facilitate the formation of the FeOOH active layer which plays a key role in enhancing the OER properties [32].

The elemental composition is determined by XPS as shown in **Table S1**. The ratio of Ni:Fe is consistent at the surface. The N peak at 398.4 eV originates from C≡N (**Figure S2**). The N/Ni and N/Fe ratios (**Table S1** and **Figure 3d**) decrease with increasing the temperature, indicating deficiency of N atoms at the surface due to formation of $V_{C\equiv N}$ [29]. According to the changes in the N:Ni ratios with temperature, the amounts of $V_{C\equiv N}$ are calculated as shown in **Figure 3e**. The $V_{C\equiv N}$ concentration increases with increasing the temperature and nearly 80% C≡N deficiency is observed on the surface after heating at 300 ºC. The regulated $V_{C\equiv N}$ in the PBAs-based electrocatalyst play an important role in the enhanced catalytic activity as well as reaction kinetics [20].

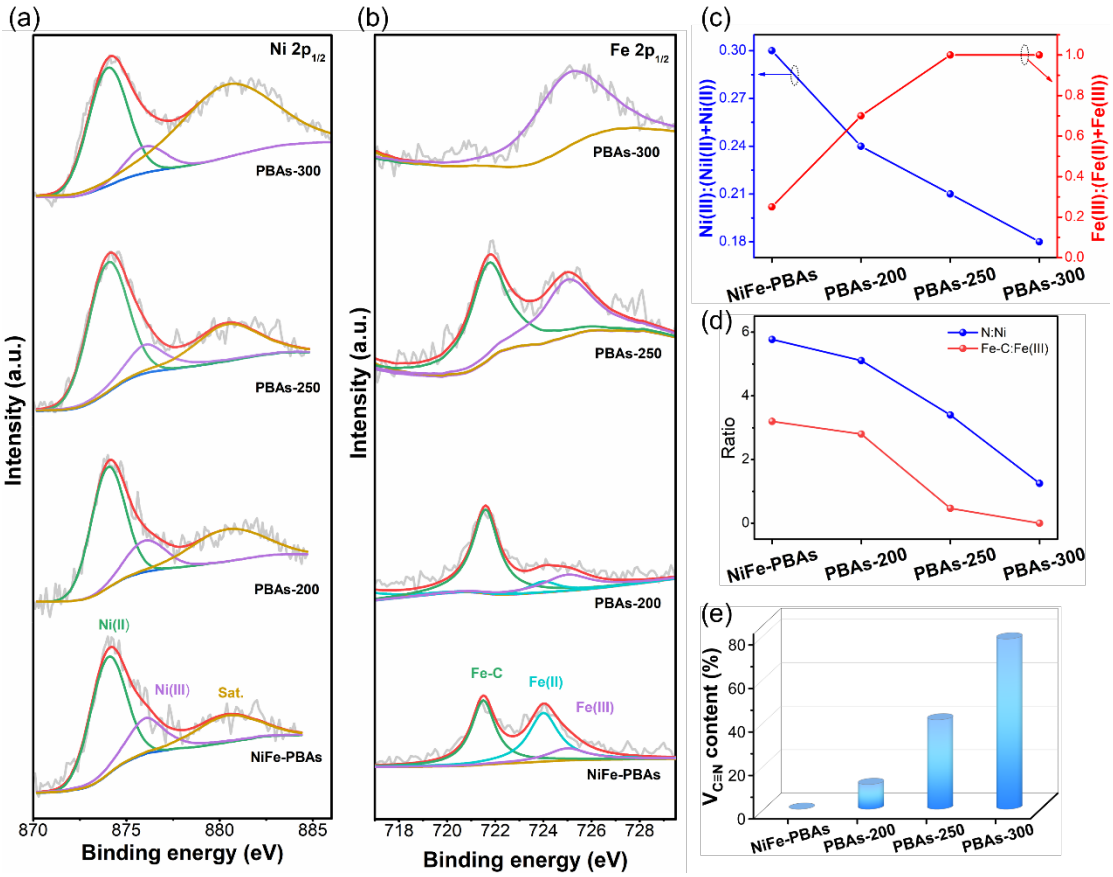

Figure 3. High-resolution XPS spectra of (a) Ni $2p_{1/2}$ and (b) Fe $2p_{1/2}$, (c) Ni(III) and Fe(III) contents, (d) Ratios of N:Ni and Fe-C:Fe(III), and (e) $V_{C\equiv N}$ contents in PBAs, PBAs-200, PBAs-250, and PBAs-300.

3.2. Electrocatalytic OER performance

The electrochemical properties of the electrocatalysts are determined using a three-electrode system in 1 M KOH. **Figure 4a** shows that the C≡N deficient electrocatalysts have smaller overpotentials than the NiFe-PBAs precursor, suggesting that $V_{C\equiv N}$ enhance the OER activity. In particular, PBAs-250 has excellent OER characteristics such as an overpotential of only 270 mV for a large current density of 50 mA cm^{-2}, which is smaller than those of PBAs-200 (342 mV) and PBAs-300 (312 mV). The improvement of PBAs-250 compared to PBAs-200 can be attributed to

more $V_{C\equiv N}$ which modify the electronic configuration and facilitate surface reconstruction of Fe active sites. However, the inferior performance of PBAs-300 with excess $V_{C\equiv N}$ compared to PBAs-250 may stem from structural damage and electron transfer impediment caused by too many vacancies and defects [25].

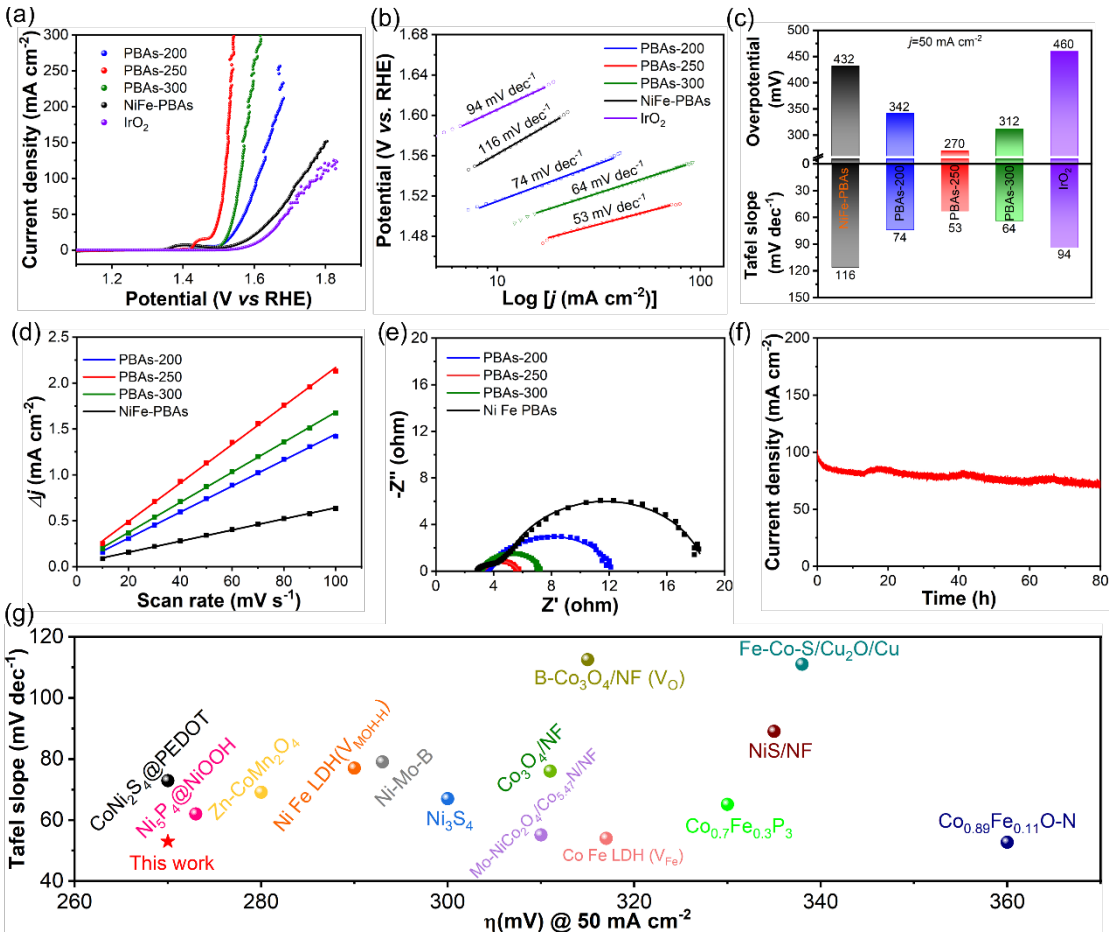

Figure 4. Electrochemical characteristics of the electrocatalysts: (a) Polarization curves, (b) Tafel plots (c) Comparison of the overpotentials at 50 mA cm^{-2} and Tafel slopes, (d) ECSA, (e) EIS, (f) Stability test of PBAs-250 at a constant current density of 100 mA cm^{-2} in 1 M KOH, and (g) Comparison of the overpotentials at 50 mA cm^{-2} and Tafel slopes with those of previously reported OER catalysts.

Figure 4b shows that the Tafel slopes of the C≡N deficient PBAs electrocatalysts are smaller than that of the NiFe-PBAs precursor, indicating that introduction of $V_{C\equiv N}$ into PBAs improves the OER kinetics. The Tafel slope of PBAs-250 is 53 mV dec^{-1} and less than those of PBAs-200 (74 mV dec^{-1}) and PBAs-300 (64 mV dec^{-1}), implying faster reaction kinetics and lower charge and mass transport barriers in OER if the amount of $V_{C\equiv N}$ is moderate (PBAs-250). However, too many $V_{C\equiv N}$ retard the OER kinetics due to electron trapping by C≡N defects. **Figure 4c** compares the overpotentials at 50 mA cm^{-2} and Tafel slopes of different electrocatalysts corroborating the excellent properties of PBAs-250 in OER.

The electrochemical active surface area (ESCA) is derived based on the electrochemical double-layer capacitance (C_{dl}), as shown in **Figures S3 and 4d**. PBAs-250 has the highest C_{dl} of 20.9 mF cm^{-2} compared to NiFe-PBAs (6.1 mF cm^{-2}), PBAs-200 (14.1 mF cm^{-2}), and PBAs-300 (16.4 mF cm^{-2}). Generally, the larger the ECSA, the more are the exposed active sites and the higher is the electrocatalytic activity. The large ECSA of PBAs-250 stems from the synergistic effect of $V_{C\equiv N}$ and Ni-Fe electronic interactions. The charge transfer resistance (R_{ct}) is determined by electrochemical impedance spectroscopy (EIS), as shown in **Figure 4e**. PBAs-250 has the smallest R_{ct} of 2.7 Ω compared to NiFe-PBAs (15.2 Ω), PBAs-200 (9.1 Ω), and PBAs-300 (4.2 Ω). The results reveal fast charge transfer with a moderate amount of $V_{C\equiv N}$.

Stability is an important parameter in practice and chronopotentiometry (CP) is performed at a high current density of 100 mA cm^{-2} for more than 80 h and **Figure 4f**

indicates that PBAs-250 has outstanding stability. Formation of $V_{C\equiv N}$ generates a large number of unsaturated Fe sites around the vacancies and the unsaturated Fe sites are more likely to reconstruct and form the FeOOH active layer during OER rather than being etched by OH^-, thereby giving rise to the excellent stability [33, 34]. **Figure 4g** illustrated the comparison of the overpotentials at 50 mA cm^{-2} and Tafel slopes with those of previously reported OER catalysts including NiFe LDH [35], Ni-Mo-B [36], Ni_3S_4 [37], Co_3O_4/NF [38], B-Co_3O_4/NF [39], Mo-$NiCo_2O_4$/$Co_{5.47}N$/NF [40], CoFe LDH [41], $Co_{0.7}Fe_{0.3}P_3$ [42], NiS/NF [43], Fe-Co-S/Cu_2O/Cu [44], $Co_{0.89}Fe_{0.11}O$-N [45], $CoNi_2S_4$@PEDOE [46], Ni_5P_4@NiOOH [47], and Zn-$CoMn_2O_4$ [48]. The morphology and composition of PBAs-250 before and after the durability test are investigated. **Figure 5a** shows that the nanocube morphology remains although the surface becomes rough due to some surface reconstruction during OER [49]. **Figure 5b** indicates conversion from Fe^{2+} into Fe^{3+} after long-term OER on account of surface reconstruction and formation of FeOOH [8, 10].

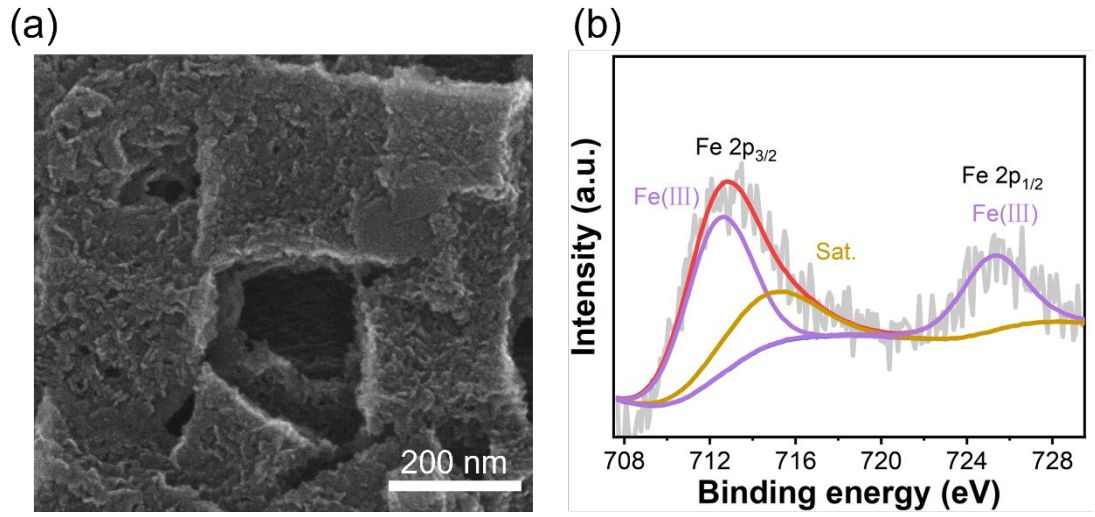

Figure 5. (a) SEM image and Fe 2p XPS spectrum of PBAs-250 after the long-term

test.

The Faradaic efficiency of PBAs-250 in OER is determined by the water displacement method as illustrated in **Figure 6a**. 43.5 mL of O_2 are generated in 120 min at a current of 100 mA (**Figure 6b**) and the Faradaic efficiency is calculated to be 95.4% which is close to 100%. It can thus be concluded that the NiFe-PBAs-based electrocatalyst with the appropriate amount of $V_{C\equiv N}$ is an excellent OER electrocatalyst. To further explore the overall water splitting performance of PBAs-250 electrocatalyst, a two-electrode system composed of the commercial Pt/C modified CC electrode (Pt/C/CC) as the cathode and PBAs-250 as anode is assembled, as shown in **Figure 6c**. **Figure 6d** shows that the cell requires a low voltage of 1.54 V for a current density of 10 mA cm^{-2}, which is smaller than those of similar Ni-based electrocatalysts listed in **Table S3**.

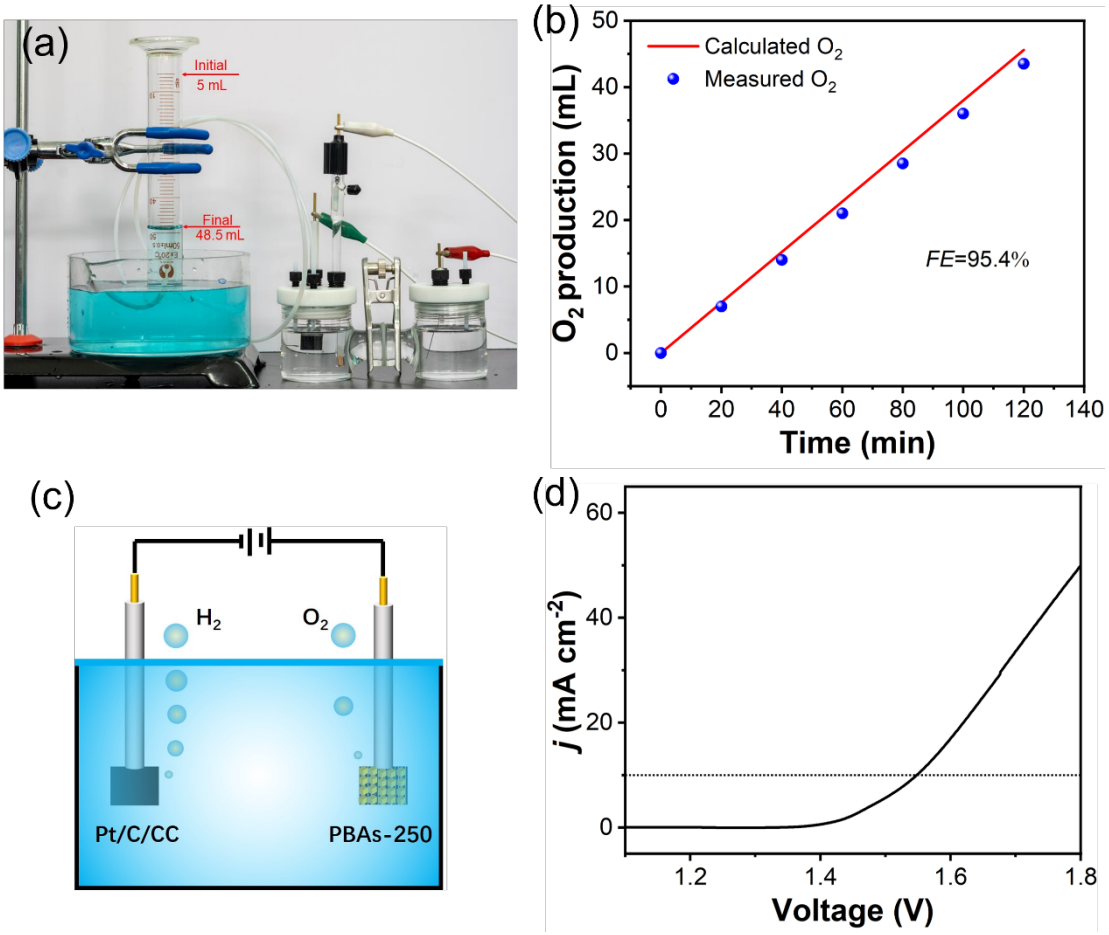

Figure 6. (a) Photograph of the OER system consisting of the PBAs-250 electrocatalyst with O_2 gas generation determined by the water displacement method, (b) Experimental and theoretical amounts of O_2 produced by the PBAs-250 electrocatalyst at a current of 100 mA in 1 M KOH, (c) Schematic showing the overall reaction in the apparatus consisting of the Pt/C/CC cathode and PBAs-250 anode, and (d) Polarization curve of the overall reaction.

3.3. Extend to other PBAs

The concept of $V_{C\equiv N}$ introduction and regulation can be extended to other PBAs-based materials. NiCo-PBAs nanocubes are prepared by the same protocol and the nanocube morphology is maintained after the thermal treatment as shown in **Figure S4**.

Figure 7a shows the crystal structure of the NiCo-PBAs precursor and thermally treated electrocatalyst (NiCo-PBAs-V), both can be indexed to $Ni_3[Co(CN)_6]_2$ (JCPDS Card No. 89-3738). After the thermal treatment, $V_{C\equiv N}$ are formed as revealed by the Raman scattering spectra in **Figure 7b**, which shows weakened C≡N vibration peaks at 2,190 and 2,208 cm^{-1} [50]. The C≡N deficient NiCo-PBAs-V electrocatalyst shows smaller overpotential and Tafel slope than the NiCo-PBAs precursor, as shown in **Figures 7c, d**. **Figures S5** and **7e** disclose that the ECSA of the C≡N deficient NiCo-PBAs-V is enlarged by 16% compared to the precursor because of the $V_{C\equiv N}$ and activation of active sites. The smaller charge transfer resistance disclosed by EIS in **Figure 7f** of the NiCo-PBAs-V confirms the fast reaction kinetics.

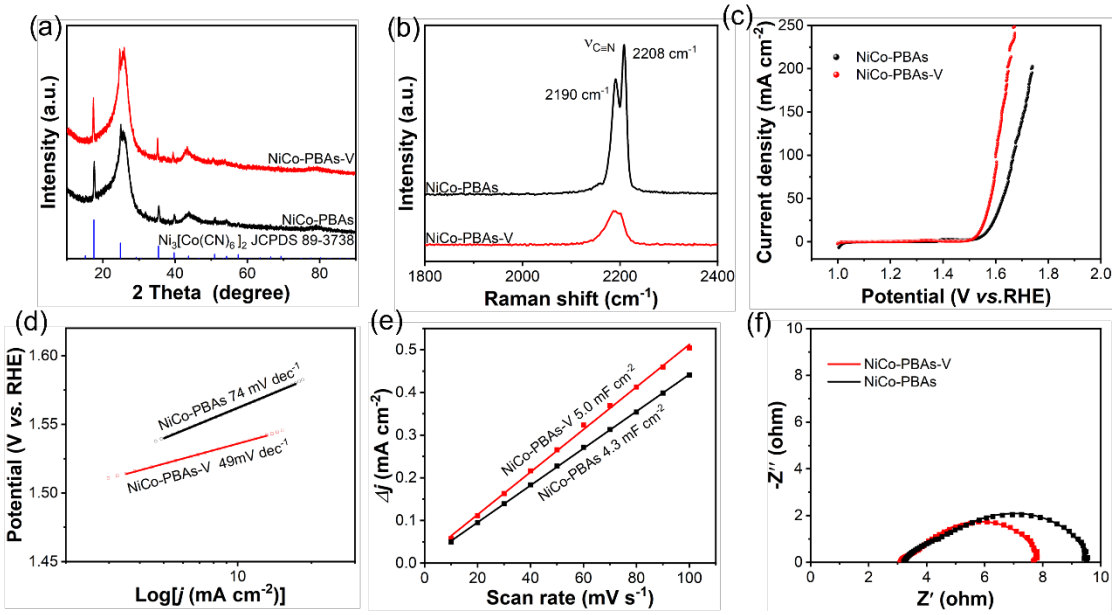

Figure 7. (a) XRD patterns, (b) Raman scattering spectra, (c) Polarization curves, (d) Tafel plots, (e) ECSA, and (f) EIS of NiCo-PBAs and NiCo-PBAs-V.

4. Conclusions

A precise regulating strategy to tune the $V_{C\equiv N}$ content in NiFe- and NiCo-PBAs for enhanced OER is described. The amount of $V_{C\equiv N}$ can be tuned precisely by thermal treatment of the electrocatalysts. $V_{C\equiv N}$ not only modulates the local electronic structure of the metal sites, but also creates unsaturated Fe sites to facilitate the formation of a catalytically active phase. The electronic interactions between Ni and Fe sites further optimize the electronic structure of the active sites for OER. Furthermore, the $V_{C\equiv N}$ restrains etching of the catalyst during OER to present outstanding long-term stability. As a result, the $V_{C\equiv N}$ modified NiFe-PBAs electrocatalyst has excellent OER characteristics such as a low overpotential of 270 mV at 50 mA cm^{-2} and outstanding stability for 80 h in an alkaline solution. The $V_{C\equiv N}$ deficient NiFe-PBAs also shows a small voltage of 1.54 V at 10 mA cm^{-2} in overall water splitting with the commercial Pt/C catalyst as the cathode in 1 M KOH electrolyte. The results suggest the improved energy conversion efficiency has been achieved by precisely regulating the $V_{C\equiv N}$ deficient in NiFe-PBAs. Our work provides insights into modification of PBAs for advanced OER and energy efficient hydrogen production.

Acknowledgments

This work was financially supported by the Key Research and Development Program of Hubei Province (2021BAA208), National Natural Science Foundation of China (52002294), Knowledge Innovation Program of Wuhan-Shuguang Project (2022010801020364), City University of Hong Kong Donation Research Grant (DON-RMG 9229021), City University of Hong Kong Donation Grant (9220061), and City

University of Hong Kong Strategic Research Grant (SRG) (7005505).

References

[1] H. Ding, H. Liu, W. Chu, C. Wu, Y. Xie, Structural transformation of heterogeneous materials for electrocatalytic oxygen evolution reaction, Chem. Rev., 121 (2021) 13174.

[2] X. Peng, Y. Yan, X. Jin, C. Huang, W. Jin, B. Gao, P.K. Chu, Recent advance and prospectives of electrocatalysts based on transition metal selenides for efficient water splitting, Nano Energy, 78 (2020) 105234.

[3] L. Xiong, Y. Qiu, X. Peng, Z. Liu, P.K. Chu, Electronic structural engineering of transition metal-based electrocatalysts for the hydrogen evolution reaction, Nano Energy, 104 (2022) 107882.

[4] J. Wang, S.-J. Kim, J. Liu, Y. Gao, S. Choi, J. Han, H. Shin, S. Jo, J. Kim, F. Ciucci, H. Kim, Q. Li, W. Yang, X. Long, S. Yang, S.-P. Cho, K.H. Chae, M.G. Kim, H. Kim, J. Lim, Redirecting dynamic surface restructuring of a layered transition metal oxide catalyst for superior water oxidation, Nat. Catal., 4 (2021) 212.

[5] S. Anantharaj, S. Noda, V.R. Jothi, S. Yi, M. Driess, P.W. Menezes, Strategies and perspectives to catch the missing pieces in energy-efficient hydrogen evolution reaction in alkaline media, Angew. Chem. Int. Ed., 60 (2021) 18981.

[6] X. Peng, X. Jin, B. Gao, Z. Liu, P.K. Chu, Strategies to improve cobalt-based electrocatalysts for electrochemical water splitting, J. Catal., 398 (2021) 54.

[7] D. Zhou, P. Li, X. Lin, A. McKinley, Y. Kuang, W. Liu, W.-F. Lin, X. Sun, X. Duan, Layered double hydroxide-based electrocatalysts for the oxygen evolution reaction:

identification and tailoring of active sites, and superaerophobic nanoarray electrode assembly, Chem. Soc. Rev., 50 (2021) 8790.

[8] X. Peng, X. Jin, N. Liu, P. Wang, Z. Liu, B. Gao, L. Hu, P.K. Chu, A high-performance electrocatalyst composed of nickel clusters encapsulated with a carbon network on TiN nanaowire arrays for the oxygen evolution reaction, Appl. Surf. Sci., 567 (2021) 150779.

[9] J. Tang, J. Xu, Z. Ye, X. Li, J. Luo, Microwave sintered porous CoCrFeNiMo high entropy alloy as an efficient electrocatalyst for alkaline oxygen evolution reaction, J. Mater. Sci. Technol., 79 (2021) 171.

[10] X. Peng, S. Xie, X. Wang, C. Pi, Z. Liu, B. Gao, L. Hu, W. Xiao, P.K. Chu, Energy-saving hydrogen production by methanol oxidation reaction coupled hydrogen evolution reaction co-catalyzed by phase separation induced heterostructure, J. Mater. Chem. A, 10 (2022) 20761.

[11] X. Peng, Y. Yan, S. Xiong, Y. Miao, J. Wen, Z. Liu, B. Gao, L. Hu, P.K. Chu, Se-$NiSe_2$ hybrid nanosheet arrays with self-regulated elemental Se for efficient alkaline water splitting, J. Mater. Sci. Technol., 118 (2022) 136.

[12] S. Xie, Y. Yan, S. Lai, J. He, Z. Liu, B. Gao, M. Javanbakht, X. Peng, P.K. Chu, Ni^{3+}-enriched nickel-based electrocatalysts for superior electrocatalytic water oxidation, Appl. Surf. Sci., 605 (2022) 154743.

[13] Y. Li, L. Hu, W. Zheng, X. Peng, M. Liu, P.K. Chu, L.Y.S. Lee, Ni/Co-based nanosheet arrays for efficient oxygen evolution reaction, Nano Energy, 52 (2018) 360.

[14] A. Qayum, X. Peng, J. Yuan, Y. Qu, J. Zhou, Z. Huang, H. Xia, Z. Liu, D.Q. Tan,

P.K. Chu, F. Lu, L. Hu, Highly durable and efficient Ni-FeO_x/$FeNi_3$ electrocatalysts synthesized by a facile in situ combustion-based method for overall water splitting with large current densities, ACS Appl. Mater. Interfaces, 14 (2022) 27842.

[15] M.B. Zakaria, T. Chikyow, Recent advances in Prussian blue and Prussian blue analogues: Synthesis and thermal treatments, Coord. Chem. Rev., 352 (2017) 328.

[16] L.M. Cao, D. Lu, D.C. Zhong, T.B. Lu, Prussian blue analogues and their derived nanomaterials for electrocatalytic water splitting, Coord. Chem. Rev., 407 (2020) 213156.

[17] J. Nai, J. Zhang, X.W. Lou, Construction of single-crystalline Prussian blue analog hollow nanostructures with tailorable topologies, Chem, 4 (2018) 1967.

[18] H. Liao, X. Guo, Y. Hou, H. Liang, Z. Zhou, H. Yang, Construction of defect-rich Ni-Fe-doped $K_{0.23}MnO_2$ cubic nanoflowers via etching Prussian blue analogue for efficient overall water splitting, Small, 16 (2020) 1905223.

[19] Z.P. Wu, H. Zhang, S. Zuo, Y. Wang, S.L. Zhang, J. Zhang, S.Q. Zang, X.W. Lou, Manipulating the local coordination and electronic structures for efficient electrocatalytic oxygen evolution, Adv. Mater., 33 (2021) 2103004.

[20] Z.-Y. Yu, Y. Duan, J.D. Liu, Y. Chen, X.K. Liu, W. Liu, T. Ma, Y. Li, X.S. Zheng, T. Yao, Unconventional CN vacancies suppress iron-leaching in Prussian blue analogue pre-catalyst for boosted oxygen evolution catalysis, Nat. Commun., 10 (2019) 2799.

[21] Y. Kang, S. Wang, K.S. Hui, H.F. Li, F. Liang, X.L. Wu, Q. Zhang, W. Zhou, L. Chen, F. Chen, K.N. Hui, $[Fe(CN)_6]$ vacancy-boosting oxygen evolution activity of Co-based Prussian blue analogues for hybrid sodium-air battery, Mater. Today Energy, 20

(2021) 100572.

[22] X. Wang, Y. Zhang, H. Si, Q. Zhang, J. Wu, L. Gao, X. Wei, Y. Sun, Q. Liao, Z. Zhang, K. Ammarah, L. Gu, Z. Kang, Y. Zhang, Single-atom vacancy defect to trigger high-efficiency hydrogen evolution of MoS_2, J. Am. Chem. Soc., 142 (2020) 4298.

[23] L. Zhang, C. Lu, F. Ye, R. Pang, Y. Liu, Z. Wu, Z. Shao, Z. Sun, L. Hu, Selenic acid etching assisted vacancy engineering for designing highly active electrocatalysts toward the oxygen evolution reaction, Adv. Mater., 33 (2021) 2007523.

[24] X. Yang, Y. Luo, J. Li, H. Wang, Y. Song, J. Li, Z. Guo, Tuning mixed electronic/ionic conductivity of 2D $CdPS_3$ nanosheets as an anode material by synergistic intercalation and vacancy engineering, Adv. Funct. Mater., 32 (2022) 2112169.

[25] C. Lai, H. Li, Y. Sheng, M. Zhou, W. Wang, M. Gong, K. Wang, K. Jiang, 3D Spatial combination of CN vacancy-mediated NiFe-PBA with N-doped carbon nanofibers network toward free-standing bifunctional electrode for Zn-air batteries, Adv. Sci., 9 (2022) 2105925.

[26] L. Han, X.Y. Yu, X.W. Lou, Formation of Prussian-blue-analog nanocages via a direct etching method and their conversion into Ni-Co-mixed oxide for enhanced oxygen evolution, Adv. Mater., 28 (2016) 4601.

[27] J. Nai, B.Y. Guan, L. Yu, X.W. Lou, Oriented assembly of anisotropic nanoparticles into frame-like superstructures, Sci. Adv., 3 (2017) e1700732.

[28] Q. Hu, X. Huang, Z. Wang, G. Li, Z. Han, H. Yang, P. Liao, X. Ren, Q. Zhang, J. Liu, C. He, Slower removing ligands of metal organic frameworks enables higher

electrocatalytic performance of derived nanomaterials, Small, 16 (2020) 2002210.

[29] H. Yang, J. Liu, Z. Chen, R. Wang, B. Fei, H. Liu, Y. Guo, R. Wu, Unconventional bi-vacancies activating inert Prussian blue analogues nanocubes for efficient hydrogen evolution, Chem. Eng. J., 420 (2021) 127671.

[30] M. Jiang, X. Fan, S. Cao, Z. Wang, Z. Yang, W. Zhang, Thermally activated carbon–nitrogen vacancies in double-shelled NiFe Prussian blue analogue nanocages for enhanced electrocatalytic oxygen evolution, J. Mater. Chem. A, 9 (2021) 12734.

[31] S. Wheeler, I. Capone, S. Day, C. Tang, M. Pasta, Low-potential Prussian blue analogues for sodium-ion batteries: Manganese hexacyanochromate, Chem. Mater., 31 (2019) 2619.

[32] K. Wang, H. Du, S. He, L. Liu, K. Yang, J. Sun, Y. Liu, Z. Du, L. Xie, W. Ai, W. Huang, Kinetically controlled, scalable synthesis of γ-FeOOH nanosheet arrays on nickel foam toward efficient oxygen evolution: The key role of in-situ-generated γ-NiOOH, Adv. Mater., 33 (2021) 2005587.

[33] L. Han, P. Tang, Á. Reyes-Carmona, B. Rodríguez-García, M. Torréns, J.R. Morante, J. Arbiol, J.R. Galan-Mascaros, Enhanced activity and acid pH stability of Prussian blue-type oxygen evolution electrocatalysts processed by chemical etching, J. Am. Chem. Soc., 138 (2016) 16037.

[34] X. Su, Y. Wang, J. Zhou, S. Gu, J. Li, S. Zhang, Operando spectroscopic identification of active sites in NiFe Prussian blue analogues as electrocatalysts: Activation of oxygen atoms for oxygen evolution reaction, J. Am. Chem. Soc., 140 (2018) 11286.

[35] Y. Wu, J. Yang, T. Tu, W. Li, P. Zhang, Y. Zhou, J. Li, J. Li, S. Sun, Evolution of cationic vacancy defects: A motif for surface restructuration of OER precatalyst, Angew. Chem. Int. Ed., 60 (2021) 26829.

[36] H. Liu, X. Li, L. Chen, X. Zhu, P. Dong, M.O.L. Chee, M. Ye, Y. Guo, J. Shen, Monolithic Ni-Mo-B bifunctional electrode for large current water splitting, Adv. Funct. Mater., 32 (2022) 2107308.

[37] K. Wan, J. Luo, C. Zhou, T. Zhang, J. Arbiol, X. Lu, B.-W. Mao, X. Zhang, J. Fransaer, Hierarchical porous Ni_3S_4 with enriched high-valence Ni sites as a robust electrocatalyst for efficient oxygen evolution reaction, Adv. Funct. Mater., 29 (2019) 1900315.

[38] D. Tang, Y. Ma, Y. Liu, K. Wang, Z. Liu, W. Li, J. Li, Amorphous three-dimensional porous Co_3O_4 nanowire network toward superior OER catalysis by lithium-induced, J. Alloys Compd., 893 (2022) 162287.

[39] H. Yuan, S. Wang, Z. Ma, M. Kundu, B. Tang, J. Li, X. Wang, Oxygen vacancies engineered self-supported B doped Co_3O_4 nanowires as an efficient multifunctional catalyst for electrochemical water splitting and hydrolysis of sodium borohydride, Chem. Eng. J., 404 (2021) 126474.

[40] W. Liu, L. Yu, R. Yin, X. Xu, J. Feng, X. Jiang, D. Zheng, X. Gao, X. Gao, W. Que, P. Ruan, F. Wu, W. Shi, X. Cao, Non-3d metal modulation of a 2D Ni–Co heterostructure array as multifunctional electrocatalyst for portable overall water splitting, Small, 16 (2020) 1906775.

[41] Z. Kong, J. Chen, X. Wang, X. Long, X. She, D. Li, D. Yang, Cation vacancy

driven efficient CoFe-LDH-based electrocatalysts for water splitting and Zn-air batteries, Mater. Adv., 2 (2021) 7932.

[42] L. Lin, Q. Fu, Y. Han, J. Wang, X. Zhang, Y. Zhang, C. Hu, Z. Liu, Y. Sui, X. Wang, Fe doped skutterudite-type CoP_3 nanoneedles as efficient electrocatalysts for hydrogen and oxygen evolution in alkaline media, J. Alloys Compd., 808 (2019) 151767.

[43] W. Zhu, X. Yue, W. Zhang, S. Yu, Y. Zhang, J. Wang, J. Wang, Nickel sulfide microsphere film on Ni foam as an efficient bifunctional electrocatalyst for overall water splitting, Chem. Commun., 52 (2016) 1486.

[44] J. Sun, P. Song, H. Zhou, L. Lang, X. Shen, Y. Liu, X. Cheng, X. Fu, G. Zhu, A surface configuration strategy to hierarchical Fe-Co-S/Cu_2O/Cu electrodes for oxygen evolution in water/seawater splitting, Appl. Surf. Sci., 567 (2021) 150757.

[45] Q. Du, P. Su, Z. Cao, J. Yang, C.A.H. Price, J. Liu, Construction of N and Fe co-doped CoO/Co_xN interface for excellent OER performance, Sustain. Mater. Techno., 29 (2021) e00293.

[46] H. Liu, D. Zhao, M. Dai, X. Zhu, F. Qu, A. Umar, X. Wu, PEDOT decorated $CoNi_2S_4$ nanosheets electrode as bifunctional electrocatalyst for enhanced electrocatalysis, Chem. Eng. J., 428 (2022) 131183.

[47] T. Wang, X. Li, Y. Pang, X. Gao, Z. Kou, J. Tang, J. Wang, Unlocking the synergy of interface and oxygen vacancy by core-shell nickel phosphide@oxyhydroxide nanosheets arrays for accelerating alkaline oxygen evolution kinetics, Chem. Eng. J., 425 (2021) 131491.

[48] D. Zhao, R. Zhang, M. Dai, H. Liu, W. Jian, F.Q. Bai, X. Wu, Constructing high

efficiency $CoZn_xMn_{2-x}O_4$ electrocatalyst by regulating the electronic structure and surface reconstruction, Small, 18 (2022) 2107268.

[49] F. Ma, Q. Wu, M. Liu, L. Zheng, F. Tong, Z. Wang, P. Wang, Y. Liu, H. Cheng, Y. Dai, Z. Zheng, Y. Fan, B. Huang, Surface fluorination engineering of NiFe Prussian blue analogue derivatives for highly efficient oxygen evolution reaction, ACS Appl. Mater. Interfaces, 13 (2021) 5142.

[50] S.F. Kettle, E. Diana, E.M. Marchese, E. Boccaleri, P.L. Stanghellini, The vibrational spectra of the cyanide ligand revisited: The ν(CN) infrared and Raman spectroscopy of Prussian blue and its analogues, J. Raman Spectrosc., 42 (2011) 2006.